An image analysis method to survey the dynamics of polar protein abundance in the regulation of tip growth

Sarah Taheraly, Dmitry Ershov, Serge Dmitrieff, Nicolas Minc

An image analysis method to survey the dynamics of polar protein abundance in the regulation of tip growth

Sarah Taheraly[1,2,*], Dmitry Ershov[1,2,*], Serge Dmitrieff[1] and Nicolas Minc[1,#]

[1] Université de Paris, CNRS, Institut Jacques Monod, Paris, France

[2] Present address: Institut Curie, PSL Research University, INSERM U932, Paris, France

[3] Present address: Image Analysis Hub, Institut Pasteur, Paris, France

[*] These authors contributed equally to this work

[#] Correspondence to nicolas.minc@ijm.fr

SUMMARY STATEMENT: Large-scale time-lapse analysis of individual tip growth and polar factor abundance, in yeast and fungi reveals limits to tip surface expansion rates, independent of local remodeling activity.

ABSTRACT:

Tip growth is critical for the life style of many walled cells. In yeast and fungi, this process is typically associated with the vectorial deposition of conserved tip factors, including polarity landmarks, Rho-GTPases, cytoskeleton regulators, membrane and cell wall remodelers. Because tip growth speeds may vary extensively between life cycles or species, we asked if the local amount of specific polar elements could determine or limit tip growth speeds. Using the model fission yeast, we developed a quantitative image analysis pipeline to dynamically correlate single tip elongation speeds and polar protein abundance in large data sets. We find that polarity landmarks are typically diluted by growth. In contrast, tip growth speed is positively correlated with the local amount of actin-related, secretion and cell wall remodeling factors, but, surprisingly, it exhibits long saturation plateaus above certain concentrations of those factors. Similar saturations observed for Spitzenkörper components in much faster growing fungal hyphae suggest that elements independent of canonical surface remodelers may limit single tip growth. This work provides standardized methods and resources to decipher the complex mechanisms that control cell growth.

INTRODUCTION

Cell growth is of paramount importance for cell size regulation, cytoplasmic density, as well as tissue morphogenesis (Neurohr et al., 2019; Soifer et al., 2016; Uyttewaal et al., 2012). All living cells grow, and their growth rates may vary extensively, from slow growing animal cells to fast fungal hyphae or pollen tubes (López-Franco et al., 1994; Perez-Gonzalez et al., 2019; Qin and Yang, 2011). Although the fitness advantage of different growth properties has been discussed (Di Gregorio et al., 2016; Steinberg et al., 2017; Weiss et al., 1975), the physical and biological mechanisms titrating growth speeds remain to date poorly unified. This is in part because this problem has often been studied at the population level, occulting individual cell behavior. These population analyses have shed important lights on the essential roles of global metabolic regulation, nutrient uptake or translational control (Klumpp et al., 2013; Loewith and Hall, 2011; Yuan et al., 2013). However, the growth of individual cells, ultimately implicates remodeling and expansion of their surfaces, a process rather attributed to the activity of the cytoskeleton, membrane trafficking and their regulators (Horio and Oakley, 2005; Köhli et al., 2008; Martin and Arkowitz, 2014). Thus, in general, the multiple intertwined elements that could modulate cell growth have hampered our understanding of this essential process.

Single cell growth analysis from microscopy time-lapses may represent an adequate mean to study this problem in quantitative terms. However, the complex 3D geometries of adherent animal cell models, featuring ruffles and curves, and their slow growth has rendered those analysis difficult, with only few recent reports directly documenting growth trajectories of individual cells *in vitro* (Cadart et al., 2018; Perez-Gonzalez et al., 2019; Son et al., 2012). Single walled cells such as those of yeast and fungi are admittedly better suited, given their more rapid growth, the irreversibility of their cell wall, and their simpler geometries (Köhli et al., 2008; López-Franco et al., 1994; Steinberg et al., 2017). In those cells, growth most often occurs in a polarized manner at one or several localized sites, and represents the main mean for those cells to reproduce, colonize or infect hosts (Riquelme et al., 2018). Tip growth may vary extensively in directionality and speeds among different species or even during the life cycles of one given specie (Bonazzi et al., 2014; Kinnaer et al., 2019; López-Franco et al., 1994; Martin and Arkowitz, 2014). Which elements may set or

limit tip growth speeds thus represent a fascinating problem with high relevance to the basic physiology of walled cells.

Studies in yeast and fungal hyphae have supported one dominant model in which tip growth may primarily be dictated by the cytoskeleton and secretion machineries which promote membrane and cell wall surface expansion (Köhli et al., 2008; Martin and Arkowitz, 2014). Indeed, many early experiments have shown that complete inhibition of actin, microtubules or secretion can halt growth (Ayscough et al., 1997; Horio and Oakley, 2005). In addition, more rapid growth, e.g. in more mature fungal hyphae, has been associated with higher concentrations of secretory vesicles clustered in the form of a Spitzenkörper (Köhli et al., 2008). However, some rapidly growing fungal tips do not feature a Spitzenkörper, and changes in vesicle transport rates are often only weakly correlated to increase in growth speeds (Kinnaer et al., 2019). Other models have been more centered on biophysical properties of the cytoplasm and the cell wall. Walled cells feature high internal turgor pressure on the order of 1-10atm. Turgor is thought to power growth by pushing and deforming freshly synthesized cell wall; and drastic reduction of pressure can halt growth instantaneously (Bastmeyer et al., 2002; Haupt et al., 2018; Lew, 2011; Minc et al., 2009). Because turgor is isotropic, polarized remodeling of the cell wall may render it thinner and softer thereby restricting its expansion to cell tips (Abenza et al., 2015; Davi et al., 2019; Davì et al., 2018). Mechanical properties of the cell wall dynamically titrated from the activity of synthesis and remodeling enzymes could thus contribute to set tip growth speeds. Finally, other geometrical elements such as tip diameter, or competition between growing tips have also been correlated with growth speeds (López-Franco et al., 1994), but whether those correlations are mere consequences of a modulation of the local abundance of growth-promoting factors has remained elusive (Bonazzi et al., 2015). Thus, in general, whether fastest growing tips exhibit higher amounts of cytoskeletal, membrane or cell wall regulators, or if one or several of those elements is limiting growth remain unclear.

The polar growth of the fission yeast *Schizosaccharomyces pombe*, has been extensively studied over the past decades, providing a large set of information on the function of individual tip proteins to growth and polarity, as well as mutants with characterized defects in growth patterns (Chang and Martin, 2009; Martin and Arkowitz, 2014). Those cells have cylindrical shapes and grow in length

during the cell cycle following a reproducible pattern. Upon cytokinesis and septation, cells first grow in a monopolar manner from their old end, and then switch to a bipolar growth mode after New End Take Off (NETO), during which the two growing tips share the same cytoplasm content (Baumgartner and Tolic-Norrelykke, 2009; Horváth et al., 2013; Mitchison and Nurse, 1985). In these cells, F-actin, but not microtubules, is strictly required for growth, and mutants in actin regulators, vesicle transport, components of the exocyst, or cell wall synthesis typically exhibit severe growth defects (Chang and Martin, 2009; Martin and Arkowitz, 2014). While recent studies have pointed to plausible intricate relationships between cell size, protein synthesis and global cell elongation rates in this system (Knapp et al., 2019), to date still little is understood on how individual tip growth properties may depend on the polarized recruitment of different factors that ultimately remodel the tip surface material to accommodate local expansion. In part, one difficulty has been to accurately discern individual old vs new end growth in large data sets and multiple conditions, and compute local protein abundance at each tip.

Here, we developed a semi-automated image analysis pipeline to compute and correlate the sub-cellular dynamics of tens of polar factors tagged with GFP at the locus and single tip growth speeds in populations of cycling fission yeast cells. Our analysis establishes the precise temporal variation in growth speeds of each tips, and suggests that co-exiting tips compete for a shared pool of growth-promoting material. We identify classes of factors positively and negatively correlated with tip growth speeds, and reveal important plateau limits to tip growth that are largely independent of the amount of canonical membrane and cell wall remodeling factors. Similar findings in very rapid growing tips of *Aspergillus nidulans*, suggest that such limits are likely inherent to the process of tip growth.

RESULTS

An image analysis platform to quantify single tip growth rates and tip protein abundance in cell populations

To study tip growth and cell polarity in fission yeast, we developed a semi-automated image-analysis software to measure individual tip elongation with a temporal resolution of 5 min, and a spatial resolution of ~50-100 nm, as well as to compute fluorescence intensity in different parts of each cell. This analysis is based on multi-stage spinning disk confocal time-lapse microscopy, allowing to track a relatively large number of cells (~10-15) in individual experiments. The platform for image analysis is designed for simple user access, and is provided as a package with examples and precise guidelines as supplementary material (see download link in Material and Methods). It includes steps and dedicated interfaces for: (i) time-lapse reordering; (ii) shape segmentation with multiple methods/parameters to segment cell contours based on e.g. phase contrast, DIC or fluoresecence markers; (iii) single cell isolations from a pair of dividing cell; (iv) extraction of geometrical features (length, diameters…); (v) birth scar detection; and (vi) definition of multiple regions of interests from which to quantify fluorescence (Figure S1).

For analyzing single tip growth and polarity, we first optimized time-lapse imaging conditions to achieve a high level of reproducibility and minimize photo-damage (Material and methods, Figure 1A and Figures S2A-S2B). Quantification of individual tip growth requires to reliably detect birth scars, which serve as crucial fixed fiducial marks along the cell axis. Although, phase contrast microscopy can be used to segment the whole cell contour (Bonazzi et al., 2014; Knapp et al., 2019), we found it was insufficient to properly discern scars. We thus supplemented cells and agar pads with low concentration of fluorescently labeled lectins that bind galactomannan and decorate the outer part of the cell wall (Davì et al., 2018; Horiseberger and Rosset, 1977). Lectin signal based segmentation allowed to position and track cell contours and detect birth scars through the cell cycle, and thus compute individual tip growth (Figure 1A-1B, S1E-F and S2C). Lectin addition did not affect growth and cell-cycle progression (Figure S2A-S2B), and also served to sharply mark the end of septation from the appearance of a dark band of unlabeled cell wall septum in the mid-cell (Horiseberger and Rosset, 1977). Together, these imaging methods and analysis pipeline

allowed to film and analyze several tens of individual cell tips and dynamically monitor their local growth and protein abundance profile with unprecedented precision and accuracy.

Patterns of WT growth rates during the cell cycle

We first used this method to document and study the dynamics of individual tip growth speed changes in the wild-type (WT) cell cycle. Cells were filmed during a period of ~5-6h and aligned in time, to synchronize the beginning and the end of each cell cycle with the sharp appearance of the lectin dark band, at the end of septation events (Figure 1E and Material and methods). In agreement with previous reports (Baumgartner and Tolic-Norrelykke, 2009; Mitchison and Nurse, 1985), we found that the old end (OE) grew immediately after septation in a near-linear manner reaching a near-constant growth speed plateau of 0.031 +/-0.011 µm/min after 30-50 min. The new end (NE) exhibited a different dynamic. It first displayed a short period of positive growth associated with its rapid re-inflation immediately after septation (Atilgan et al., 2015; Baumgartner and Tolic-Norrelykke, 2009). It then ceased growth, to take off *de novo* on average at around 60 min after septation, eventually reaching a short plateau at a growth speed of 0.022+/- 0.007 µm/min, significantly lower than that of the old end. As a result the total cell elongation speed, computed as the sum of both individual tips increased steadily, and reached a plateau towards the end of G2/interphase. Growth phases at both ends then sharply transited to a simultaneous deceleration about 120 min after septation, reaching complete growth cessation between 150-170 min, followed by growth resumption in the next cell cycle (Figure 1C-1D).

Patterns of individual WT tip growth were similar at 25°C and 30°C, but tips reached higher speeds at higher temperature. At 35°C, a large fraction of cells exhibited a partial monopolar phenotype with little new end growth. By comparing patterns of the laboratory WT strain with that of a prototroph strain, we found that auxotrophies did not grossly affect growth patterns and maximal growth speeds at each tip (Figure S2D). Also, in agreement with several reports, this analysis showed that the total growth speeds of WT cells steadily increased over the cell cycle, as cell size increase. As a consequence, the size-normalized growth rate was nearly constant during the cell cycle, in agreement with recent reports (Knapp et al., 2019). However, this rate computed for each single tip was not constant, and even decreased for the old end, suggesting that although global cell size could participate in setting total cell growth speeds, individual tips may be regulated by a more

local than global mechanism (Figure S2E-S2F). Finally, although the mean growth speed at each tip exhibited self-similar dynamic trends in individual cells, we noted that even among cells from the same culture and filmed at the same time, there was significant variations of up to 30-40 % in individual tip growth speeds (Figure 1D). This suggests that cell to cell variations in tip growth speeds, in addition to those along the cell cycle, may be exploited to understand tip growth regulation.

To identify the phases of the cell cycle associated with marked changes in tip growth speeds, we next computed growth while imaging markers of polarity (active GTP-Cdc42, CRIB-GFP), mitosis (tubulin, GFP-atb2), cytokinesis (Myosin light chain, rlc1-GFP), and septation (β-Glucan synthase, GFP-bgs4). This analysis confirmed that the time 0 of our growth curves corresponded to the end of septation, as evidenced by the GFP-bgs4 signal that completely filled the mid-cell (Point 0, Figure 1D and 1E). The onset of growth deceleration at both tips, corresponded to spindle assembly in metaphase, with the appearance of a small spindle and the absence of interphase microtubule bundles in the atb2-GFP signal (Point 1, Figure 1D and 1E). Interestingly, although growth began to decelerate at this point, we noted that both active-Cdc42 and Bgs4 were still mostly present at cell tips. Finally, growth completely stalled during a short period of ~10 min which corresponded to the phase of ingression of the cytokinetic ring and septum (Point 2, Figure 1D and 1E). Accordingly, both active-Cdc42 and Bgs4 became fully relocated to the mid-cell, and absent from stalled tips. Thus, entry into mitosis may trigger the progressive detachment of important polar proteins and consequent growth deceleration, with full detachment during cytokinesis and complete tip growth arrest.

Evidences for a competition for growth potential between growing tips

One interesting feature of the WT growth pattern, is that the new end never reaches the same growth speed as the old end (Figure 1D) (Mitchison and Nurse, 1985). We envisaged three putative scenarios for this: (i) the cell cycle length may not be long enough for the new end to reach the growth speed of the old end; (ii) this difference could be caused by a particular biochemistry and/or mechanics at the new end inherited from the septum (Atilgan et al., 2015; Davi et al., 2019), or (iii) that the two tips continuously compete for a limited pool of growth promoting components, and

the earlier take off of the old end segregates an initial pool at the expense of the new end, preventing it to reach the same speed.

To begin testing these hypothesis, we first studied the tip growth patterns of *cdc25-22* mutant allele cells, which spend a significantly longer time in a G2 growth phase, even at permissive temperature (25°C) (Russell and Nurse, 1986). In these cells, although the full cell cycle was much longer, NETO was delayed by a similar time as in WT (Figure 2A-2B). As a consequence, both tips expanded for periods twice longer than in WT, and reached growth speeds before mitosis slightly higher than in controls. However, in spite of this longer period, the new end reached a maximum growth speed plateau that was still significantly smaller than at the old end (Figure 2C). This suggests that the duration of growth phases may not be the main factor accounting for the differential growth speeds between the old and the new end.

Next, we built on a serendipitous observation of outliers of the default pattern in the WT population. As we tracked a large number of cells, we found that 7% of cells exhibited a delayed bipolar pattern, in which the new end took off later than in the normal WT pattern. Remarkably, in these cells, the old end reached significantly higher growth speeds than in normal WT, indicating putative competitions between the two ends (Figure 2D-2F and 2I). Conversely, 15% of WT cells exhibited a premature bipolar pattern, in which the new end took off earlier than in the majority of WT cells. In these, the old end grew significantly slower than in the default WT pattern (Figure 2D, 2G-2H and 2I). Importantly, in both outlier patterns, although the distribution of growth speeds between the two ends was markedly different than in the default pattern, the growth speed of the whole cell was nearly identical (Figure 2D-2I). Thus, these observations suggest that the two ends may compete for growth potential, and that the earlier onset of *de novo* growth at the old end may provide a competitive advantage for it to reach higher speeds.

To further test this competition hypothesis, we sought to perturb the growth pattern in a more severe manner. For this, we analyzed the growth of several *tea* mutants, *tea1Δ*, *tea3Δ* and *tea4Δ*, which have penetrant monopolar phenotypes (Chang and Martin, 2009). In these cells, tip growth was monopolar and could be either restricted to the old or to the new end (Figure 3A-3F and S3A-S3B). In all three mutants, single growing tips whether new end or old end born, could reach maximal

growth speeds that were mostly similar (Figure S3C). This observation rules out the hypothesis that inheritance of septum material at the new end could impact tip growth potential. Importantly, these individual ends grew faster that their WT counterpart. *tea1Δ* cells provided the most striking effect, because the total cell growth speed was nearly identical to that of WT cells, so that single old end grew ~1.7X faster than in WT and new ends up to 3X faster than in WT (Figure 3F). *tea3Δ* and *tea4Δ* old and new ends also grew significantly faster than in WT, but their growth speed was lower than the sum of the two ends in WT, plausibly because of secondary defects of these mutants on global processes such as metabolic activity (Figure S3C) (Kelkar and Martin, 2015). Thus, preventing growth from one tip allows the other one to reach higher growth speeds. In conclusion, growing tips sharing the same cytoplasm may compete for a limiting pool of growth-regulating factors, and the tip that takes off earlier will maintain a growth-potential advantage on the other even through long periods of growth.

Dynamics of polar protein abundance and their relationship with tip growth

The above results were indicative of the existence of a putative limiting pool of one or several growth-promoting factors shared between tips. We envisaged those factors to localize at cell tips and have known contribution to polar growth. If a given factor is central to tip growth speeds determination, then one could expect that its tip concentration should exhibit a positive relationships with individual tip growth speeds. We thus built on our image analysis platform to extract from time-lapse movies the concentration of canonical polar proteins tagged with one or multiple GFPs at the locus. Because the global (on the whole cell) concentration, of many polar factors, has been shown to be mostly constant over the cell cycle (Knapp et al., 2019), we focused on quantifying local polar accumulation at cell tips. The fluorescence signal at cell tips was averaged on boxes of fixed sizes and normalized to that of the cytoplasm after background subtraction (Figure S1). This normalization allows to directly subtract photo-bleaching effects in the concentration dynamics at cell tips (Material and methods). In addition, cells were not necessarily filmed from the onset of septation, and were re-ordered after analysis, so that putative remaining contributions of photo-bleaching were likely smoothed out in our analysis. Finally, we note, that this measured concentration only represents a relative value, as some less abundant factors were tagged with multiple copies of GFP (Material and methods).

We first investigated the dynamics of the most upstream landmarks proteins tea1p, tea4p and pom1p, which are required for NETO (Figure 4A-4B) (Chang and Martin, 2009). In agreement with their function as landmarks promoting NETO, we found that the concentration of these factors at the new end increased over the cell cycle. For instance, Tea1-3GFP got progressively recruited to the new end after septation, and reached a saturating level typically after NETO. In sharp contrast, its concentration at the old end decreased over the cell cycle. Tea4-GFP levels were steadier at both ends with a notable progressive recruitment at the new end. Pom1-GFP concentration also decreased steadily at the old end, and exhibited a bell-shape curve first increasing and then decreasing at the new end (Figure 4C-4E). To understand if those factors could contribute to set or limit individual tip growth speeds, we extracted instantaneous tip factor concentration and growth speed from both tips of each cell, and binned them to plot the growth speed of a single tip (OE or NE) with respect to tip factor concentration. Importantly, the range of tip speeds and protein concentration in these plots reflects cell to cell variations as well as those along the cell cycle. Interestingly, this analysis indicated that tip speed was mostly independent of polarity landmarks, or that these were even less concentrated in tips that grew faster (Figure 3C-3E). Thus, this suggests that polar landmarks are rather diluted by growth than contributing to growth speed *per se*.

As F-actin is known to be essential for cell growth in *S. pombe*, we next looked at actin-regulating factors (Figure 5A). One prime upstream regulator of actin assembly is the conserved Rho-GTPase Cdc42. We filmed the probe CRIB-GFP which labels active GTP-Cdc42 (Tatebe et al., 2008). The mean dynamic of CRIB-GFP at each end over the cell cycle resembled that of the mean growth patterns, with a rising phase at the old end, followed by a plateau and a sharp decay at mitosis. At the new end, CRIB-GFP concentration slowly raised from the onset of NETO and reached a plateau of concentration at a value similar to that of the old end (Figure 5B). Accordingly, the growth speed - concentration plot exhibited a general positive correlation, with faster growing tips associated with more CRIB-GFP signal, in agreement with the well-established role of active-Cdc42 in polar growth (Martin and Arkowitz, 2014). However, we noted two unexpected features. First, the new end concentrations covered a nearly similar range as those at the old end, but with markedly slower growth speeds. Second, for each tip, the growth speed exhibited a long plateau over a 2-3 fold range of CRIB-GFP levels (Figure 5B). Thus, instantaneous tip concentration of active-Cdc42 cannot

predict tip growth speeds, with different speeds obtained from one given tip concentration, and a single maximum growth speed from a large range of concentration values.

In agreement with the results obtained for active-Cdc42, we found similar trends and dosage – dependence for the formin For3-3GFP, which nucleates actin cables and Bud6-3GFP, an actin-nucleation promoting factor (Chang and Martin, 2009). Both exhibited a dynamic loading at individual tips which resembled that of individual tip growth, and a long plateau in the growth-concentration plot, suggesting that higher recruitment of those factors cannot improve tip growth further (Figure 5C-5D). We also investigated the dynamic of F-actin using the probe LifeAct-GFP. Importantly, the signal we analyzed mostly corresponded to bright and intense actin patches which label endocytic vesicles, with only negligible contributions from actin cables. The dynamic of F-actin also resembled that of tip growth, and a clear saturation in growth speeds at both ends was evident for the largest range of F-actin tip concentration (Figure 5E). Thus, although F-actin is required for growth in those cells, its local tip concentration may not limit tip growth.

We then looked at more upstream factors involved in surface remodeling, covering processes including secretory vesicle delivery and fusion with the membrane, cell wall synthesis and integrity (Figure 6A). The type V myosin Myo52-3GFP which drives secretory vesicles to the cell tips, as well as Sec8-GFP a subunit of the exocyst complex that promotes vesicle fusion, had similar signatures as actin-related factors discussed above (Figure 6B-6C). Factors related to cell wall synthesis including the Rho-GTPase Rho1, visualized with the active probe act-Rho1-citrine, and its catalytic subunits GFP-Bgs1 and GFP-Bgs4 also exhibited similar dynamics resembling that of tip growth, with a positive correlation with tip growth and a saturation plateau. However, we noted that GFP-Bgs1, had a more linear dose-dependent trend with new end growth speeds, but still exhibited a plateau in growth speed at the old end (Figure 6D-6F). Finally, we also imaged the dynamics of Rgf1-GFP an important component of the cell wall integrity pathway, a sensing cascade that controls cell wall synthesis in response to damage (Perez and Cansado, 2010). The growth speed- concentration plots was slightly different than all other upstream cues, and appeared to exhibit the most linear trend with growth speeds at each end. Yet, the same concentration of Rgf1-GFP did not correspond to the same tip growth speed at the new vs old end, suggesting, that Rgf1 may not directly dictate growth speeds (Figure 6G). Rather, one plausible interpretation of

this curve, in line with the wall sensory function of Rgf1 is that it behaves as a sensor of growth speed changes, and accumulates or detaches in response to intrinsic changes in wall strain rates (Davì et al., 2018). In conclusion, these data strongly support that canonical cell surface remodeler are positively coupled to tip growth speed, but not directly limiting it.

Dynamics of upstream polar component in faster growing tips

To further test inherent limits to tip growth independent of canonical surface remodeling factors, we explored the dynamics of CRIB-GFP, LifeAct-GFP, Myo52-3GFP, GFP-Bgs4 and Rgf1-GFP in *tea1Δ* cells in which individual tips can grow significantly faster than in WT (Figure 3B-3F). In these monopolar cells, all above factors were solely located to the growing end (Figure 7A). However, and in agreement with results in WT, the growth-concentration curves of CRIB-GFP, LifeAct-GFP, Myo52-3GFP, GFP-Bgs4 were shifted upward with respect to WT but still saturated on a long plateau of concentration values. Thus, with a given tip concentration of F-actin or Bgs4 for instance, a single tip can typically grow 2-3 times faster (Figure 7B-7E). Rgf1-GFP dynamics further supported its putative sensing phenotype, with a near linear positive relationship with faster *tea1Δ* cells tip growth speeds (Figure 7F).

Finally, we sought to expand further the range of validity of our observation, by testing correlations between tip concentration of surface remodelers and growth speeds, in much faster growing cells. For this, we adapted our image-analysis platform to hyphal cells of the model filamentous fungus *Aspergillus nidulans*. As single tips grow rapidly and in a monopolar manner, contour-detection based on phase contrast images was sufficient to compute instantaneous growth speeds (Figure 8A-8B). As in these hyphal cells, the Spintzenkörper is an established source of local secretory vesicles needed for surface remodeling, we tracked GFP-RabE^{Rab11} which labels exocytic post-golgi vesicles and thus represents a faithful marker of Spintzenkörper dynamics and surface remodeling (Pantazopoulou et al., 2014; Peñalva et al., 2017). In *Aspergillus nidulans*, as in many fungi, tip growth typically increases with the age of the colony, and/or the length of the hyphal compartment (Horio and Oakley, 2005; López-Franco et al., 1994). We thus filmed and computed hyphal tip growth, in early germlings tubes, that emerge from germinating spores and precede the first septation, as well as more mature hyphae (Figure 8A and 8C). This allowed to span a range of ~5-10 fold in individual tip growth speeds, and almost 20-30 fold in local GFP-RabE^{Rab11}

concentration. Remarkably, the growth-concentration curve for germlings, resembled that of *S. pombe* individual cell tips, with a dose-dependence increase of tip growth with GFP-RabE^{Rab11} concentration at low and intermediate concentrations, followed by a plateau at higher concentration (Figure 8D). In mature hyphae, growth speed was constant over a plateau covering the full range of GFP-RabE^{Rab11} concentrations. Thus, this result indicates that tip growth speeds in rapid hyphal cells, as in slower yeast cells, may also be positively correlated, yet not limited by the local concentration of secretory vesicles.

DISCUSSION

A new method to study tip growth

We here developed and validated a standardized methodology to track individual trajectories of single tips while computing the abundance of fluorescently-tagged proteins. This method is based on simple confocal time-lapses, and allows to compute with medium-throughput single tip growth properties, in polar-growing cells including yeast and filamentous fungi. A first particular feature that demarks our method from previously reported tracking tool for fission yeast growth (Baumgartner and Tolic-Norrelykke, 2009; Knapp et al., 2019; Nobs and Maerkl, 2014), is that it allows the faithful detection of birth scars, thus allowing for the study of individual tip growth in the same cell. In addition, the use of multiple detection boxes allows the computation of protein abundance at cell tips, or at any location around the cell (cytoplasm, nucleus or membrane). As exemplified in this work, this approach provides unprecedented details on polar protein dynamics and single tip growth rates, their evolution over cell cycles, in multiple conditions and in relatively large cell populations. Importantly, the image analysis platform has been optimized to ensure facile user adaptation, and is readily available for the community (see download link in Material and Methods). Thus, we anticipate that this tool will help screening growth and polarity defects in large sets of mutants or fungal species, as well as allow to better document links between local or global protein abundance and morphogenetic phenotypes.

Competition for growth potential between multiple sites

Inner working designs of Cdc42-based polarity machineries allows cells to grow from one or multiple sites sharing the same cytoplasm (Das et al., 2012; Martin, 2015; Wu and Lew, 2013). This is typical in fission yeast during NETO, as well as in most filamentous fungi that undergo apical or lateral branching (Chang and Martin, 2009; Riquelme et al., 2018). While mechanisms that allow for the coexistence of competing polarity domains are beginning to be understood (Bendezu et al., 2015; Howell et al., 2009), a largely unexplored question is whether multiple sites may also compete for growth potential. By tracking single tip dynamics in outliers of the canonical fission yeast growth pattern, as well as in monopolar mutants, we reveal that growth sites sharing the same cytoplasm compete for growth potential. As a consequence, a single tip will typically grow nearly as fast as the sum of two co-growing tips, in the same background. Interestingly, this competition appears to be set by the history of growth sites, rather than by an instantaneous redistribution of growth potential. Accordingly, tips that initiate growth earlier maintain an advantage for several hours, and systematically reach higher speeds (Figure 2 and 3). In filamentous fungi, the mother filament also grows much faster than emerging lateral branches, suggesting that this effect could represent a general feature of competing growth sites (Riquelme and Bartnicki-Garcia, 2004). One plausible interpretation, is that growth initiation implicates the modification of a pre-existing non-growing membrane and cell wall, and thus consumes growth promoting factors, thereby reducing the subsequent growth potential of the tip. We do not favor this hypothesis, because monopolar mutants like *tea1Δ*, can reach similar growth speed when growing from the former septation site (new end) or the former old end. An alternative plausible scenario is that each tip can increase their growth with a similar acceleration potential, and reach a plateau in growth speeds when a putative pool of factors promoting acceleration becomes depleted. Growth acceleration could for instance be associated with positive feedbacks between growth and polarity, which have been evidenced in fission yeast (Bonazzi et al., 2014; Haupt et al., 2018). Although computing acceleration with high accuracy, as the second derivative of length evolution, is challenging in slow growing yeasts, we expect that such hypothesis could be easier to test in faster growing model fungi.

Tip growth speed determination and local abundance of polar factors

The process of tip growth is intrinsically linked with the deposition of tens of different conserved factors at cell tips. The hierarchical role of each type of proteins has been well established by

genetic studies in model yeasts and fungi (Martin and Arkowitz, 2014; Riquelme et al., 2018). First, spatial landmarks position the incipient growth site, and recruit downstream polarity components organized around the active form of Rho GTPases, such as Cdc42. Polarity platforms then localize sites of F-actin assembly, endocytosis and secretory vesicle delivery, which ultimately deliver membrane and wall remodeling factors that accommodate surface expansion. In here, by systematically documenting the dynamic loading of canonical markers of above mentioned processes, we assess how their polar concentration may contribute to and/or limit tip growth speed.

One general finding is that polarity landmarks appear to be rather diluted by growth, while other upstream elements are mostly positively correlated with growth speeds. A possibility is that these differences reflect the cytoskeletal elements that drive their polar recruitments: microtubules for polar landmarks, and F-actin for upstream factors. The positive relationship between upstream elements, such as F-actin, exocysts components or cell wall synthases, and single tip growth is consistent with recent reports demonstrating that an increase in proteome concentration may drive faster global cell growth (Knapp et al., 2019). However, one unexpected result is that these upstream elements, do not appear strictly limiting for single tip growth speed determination. This result is supported by the relatively long plateaus in growth-polarity plots for these factors (Figure 4-5), and the marked difference in tip growth speed which can be achieved with a similar range of factor concentration in WT vs monopolar *tea1Δ* cells. We note however, that a major limit inherent to our approach is that we solely imaged relatively abundant and previously characterized factors; thereby potentially omitting less expressed or yet unidentified elements that could act as crucial limiting regulators of tip growth. For instance, our trials to properly compute the dynamic of important cell wall regulators, such as glucanases or glycosyl-transferases (Davi and Minc, 2015; Perez and Ribas, 2004), failed given their low fluorescent signals. Further optimization of fluorescence tagging, with more advanced fluorophores, could potentially allow to analyze the contribution of these factors. In addition, growth limitation may also implicate post-translational modifications such as phosphorylation, which we have not investigated here.

Overall, our findings suggest that the competition for growth potential between tips, or more generally the speed determination of a single growing tip, may not solely result from a simple linear competition or loading of a given pool of polar factors. Rather these processes may implicate more

complex dynamic feedbacks inherent to polarity circuit, such as oscillations between tips (Das et al., 2012), or to cell wall rheology and assembly, which ensure surface integrity while promoting its expansion (Davì et al., 2018). Further quantitative studies of the process of cell growth will be required to decipher these complex interplays.

MATERIALS AND METHODS:

Yeast strains and media: Fission yeast *Schizosaccharomyces pombe* cells were grown at room temperature in yeast extract plus 5 supplements (YE5S) media unless otherwise indicated. Strains used in this study are listed in Table S1. For time-lapse experiments, cells were grown overnight in liquid culture at 25°C harvested, and labeled during 5min with 5 mg/ml of fluorecsent lectin-A647 from *Griffonia simplicifolia* (alias *Bandeiraea simplicifolia*) Gs-IB4-Alexafluor647 (ThermoFisher), and mounted on an agar pas supplemented with 5 mg/ml of Lectin-A647 and imaged directly (Davì et al., 2018).

Fungi strain and media: A mycelium of *Aspergillus nidulans* was grown for 5 days on Malt Extract (MCA, Aspergillus complete medium) plates, and spores were collected in water supplemented with 1% tween 20%, and kept at 4°C, for up to a month. For time-lapse imaging, a 1/10 dilution of spores was plated on a cellophane on top of an MCA agar plate and grown overnight at 25°C. The next morning, a square of cellophane (~15 x 15 mm^2) was cut and placed on a MCA agar pad supplemented with 0.2mg/ml of fluorescent WGA lectin (Wheat germ agglutinin-AlexFluor 647, ThermoFisher).

Microscopy: Live-cell imaging was performed on an inverted spinning-disk confocal microscope equipped with motorized stages and perfect focus system (Nikon Ti-Eclipse), a Yokogawa CSU-X1FW spinning head, an EM-CCD camera (Hamamatsu), a 100× oil-immersion objective (Nikon CFI Plan Apo DM 100×/1.4 NA) and a 2.5× magnifying lens, and controlled by MetaMorph® (Microscopy Automation & Image Analysis Software). For yeast experiments, time-lapses were approximately 5 to 6 hours long with an interval of 5 or 10 min (depending on the strain). Exposure in the Blue or Far-Red channels were kept similar between experiments, to homogenize putative phototoxic effects and bleaching. However, in some of the dimmer signals, we increased both the exposure and time intervals, so that the total amount of light received by cells was roughly constant. Imaging was performed at room temperature (22-26°C) unless indicated otherwise, with controlled humidity (>30%). For experiments on *Aspergillus nidulans*, the objective was heated up at 28°C with an objective heater (Bioptechs).

Image analysis: To analyze single tip growth rates and local concentrations of polar factors we improved a previously reported dedicated MATLAB (Mathworks) image-analysis platform (Davì et al., 2018; Haupt et al., 2018) (Figure S1). We first segmented cells using the signal from the lectin-labeled cell wall. To this aim, we first smoothed the image with median and Gaussian filters and detected cell edges using the Canny edge detector. The resultant binary image was then filtered to remove small edge chunks. Given that the signal of the labeled cell wall has a finite thickness, the edges delineated the inner and the outer border of this signal. All spaces in this image were then filled in white (binary 1) except for the spaces between the inner and outer border of the wall, yielding a black band (binary 0) representing the cell wall. Using the watershed algorithm, we finally extracted the whole-cell contour defined as the middle of this band. Note that in the platform a dedicated interface allows to modulate these segmentation steps, in order to segment different types of signals (Phase, DIC, fluorescence…). To compute cell length, we fitted the long axis of the segmented cell with a polynomial of degree 3. This fit was then used to define a ‘‘cell spine’’ and its length was calculated and used as a measurement for cell length. An interface then allows to define more precisely the cell shape, remove unwanted neighbor cells or objects and orient the NE vs OE. The final step consists of adjusting the spine and tracking the birth scars by a semi-automated interface, based on radius detection along the cell spine, and manual verification of scar positions. The positions of scars allow for the computation of elongation rates of the NE and OE.

The whole-cell contour could then be manipulated using morphological and logical operations to obtain a set of arbitrary regions (tips, membrane, cytoplasm, etc…). The tip regions are for instance shaped as a cut off from the whole-cell mask perpendicular to the cell spine at specific distances along the spine. The background was calculated from a region surrounding the cell shape defined by dilation of the cell shape. Fluorescent signals of interest were then extracted from fluorescent images by using a mask based on corresponding sub-regions and were background corrected. The concentration at cell tips was computed by normalizing the background-corrected tip signal with the background-corrected cytoplasm signal; allowing to directly account for photobleaching effects.

This tracking platform is available for the community. The following download link provides a package including the image analysis method for tracking growth and polarity, precise user-friendly guidelines and examples for training:

https://drive.google.com/file/d/1Fot7V0PvoFGXnYBSZMsWgEiuPIWjY6Kz/view

Finally, a second dedicated Matlab script was developed to compute the mean trend in cell size, tip growth speed and pole concentration over a population of single tips analyzed from the tracking platform mentioned above. Because cell cycle time can vary even within the same group of cells imaged at the same time; we rescaled the cell cycle time of each cell to the average cycle time of the genetic background.

To obtain averaged measurements (total length, OE/NE lengths, OE/NE concentrations values) and their derivatives (growth speed and growth rate, computed as a local slope over a 3 points window) over multiple cells, we binned time in bins of 10 minutes, in order to compute the mean behavior of the population in each bin, and the standard deviation (see Figure 1C and 1D, for example).

To plot tip growth speed as a function of pole concentration, we used the data from individual (non-averaged) cells. We binned concentration in a set of thirty regularly spaced bins of concentration between 0 and the maximum observed concentration, and discarded bins that had less than five experimental time-point to limit outlier behavior. In each bin, we then computed the mean and the standard deviation of tip growth speed.

Statistical and correlation analyses were carried out using Prism 6 software (GraphPad Software, La Jolla, CA). To compute significance throughout this work, we used one-way analysis of variance (ANOVA) followed by Dunnett multiple comparisons test or two-tailed, unpaired t test. Statistically significant difference between groups is reported in figure legends. For all experiments reported in this study, at least two independent experiments were performed.

ACKNOWLEDGMENTS

We thank the Martin, Gould, Tran/Paoletti, Wu, Sanchez, Balasubramanian, Chang and Peñalva labs for sharing strains and reagents. We gratefully thank all members of the Minc lab for discussion and technical help.

COMPETING INTERESTS

No competing interests declared

FUNDING

This work was supported by the Centre National de la Recherche Scientifique (CNRS), the Agence Nationale pour la Recherche ("Cell size" no. ANR-14-CE11-0009-02) and the European Research Council (ERC CoG "Forcaster" no. 647073).

FIGURE LEGENDS

Figure 1. An image analysis platform to extract single tip growth trajectories in fission yeast. (A) (*Left*) Schematic representation of a fission yeast cell with 2 birth scars. The green area corresponds to the old end (OE) and the red area to the new end (NE). (*Middle*) By defining the scars from the local radius along the cell axis, (colored dots at cell sides), the software extracts the evolution of each individual tip growth speed. (*Right*). Typical modular boxes based on the segmentation of the cell shape, which serve to compute local levels of fluorescence around the cell. **(B)** Time-lapse example of a WT cell segmented and tracked by the software. Note how birth scars position remains stable during growth over the cell cycle. (**C)** Length differences of growing OE, NE and total cell of WT cells tracked every 5min over the cell cycle. The dark line represents the average, and colored shades delimit +/- the standard deviation (n=73 cells tracked from 5 independent experiments). **(D)** Instantaneous growth speeds, for the same set of cells as in 1C, computed as local derivatives of length evolution curves. The important transitions in growth speeds (0, 1 and 2) are marked in this graph and correspond to images presented in 1E. Stage 0 represents the end of septation, stage 1 is the maximum growth speed point, and stage 2 the lowest growth speed point. **(E)** Localization of typical markers of the cell wall, mitosis, polarity, septation and cytokinesis at key transition stages in growth speeds (as indicated in 1D) at +/- 150 sec of each stage. Stage 0 marks the end of septation, as seen by the appearance of a dark band in the lectin signal, and GFP-bgs4, decorating the full septum space. Stage 1 marks entry in mitosis as seen in the GFP-atb2 (Microtubules) channel. Stage 2 corresponds to the initiation of cytokinesis as seen in the CRIB-GFP, GFP-bgs4 and rlc1-GFP channels. Scale bars, 5µm.

Figure 2. Evidences of a competition for growth potential between tips sharing the same cytoplasm. (A-B) Comparison of Total, OE and NE lengths expansions and Growth Speed (GS) of WT (dotted lines, n=73 cells) and *cdc25-22* (full line, n=24 cells) cells during their respective

cell cycle. **(C)** Mean maximum growth speed, computed as an average on 20min around the maximum of the speed profile, for the OE and NE of WT and *cdc25-22*. **(D)** Cell cycle time-lapses, segmented and analyzed with our software, comparing delayed and premature bipolar patterns, with canonical WT growing cells. The green and red lines compare growth at the OE and the NE respectively, and black dotted lines highlight differences in growth. **(E-H)** Length expansions and growth speeds over the cell cycle of WT cells undergoing delayed (E-F, n=5 cells) and premature bipolar (G-H, n=11 cells) pattern compared to the standard WT pattern (n=73 cells). **(I)** Mean maximum growth speed, for delayed, normal and premature bipolar cells, for the OE, NE and total. Results were compared by using a two-tailed Mann–Whitney test. *, $P < 0.1$; **, $P < 0.01$; ***, $P < 0.001$. Error bars are standard deviations. Scale bars, 5µm.

Figure 3. Competitions for growth potential between tips evidenced in monopolar mutants **(A)** Time-lapse of *tea1Δ* cells labeled with LectinA647, with one daughter growing exclusively from the OE, and one from the NE. **(B-E)** Length expansion and related growth speeds of *tea1Δ* cells growing from the NE only (n=35 cells, **B-C**) or the NE only (n=16 cells, **D-E**), compared with WT cells (n=73 cells). **(F)** Mean maximum growth speed for OE, NE and total length of *tea1Δ* vs WT cells. Results were compared by using a two-tailed Mann–Whitney test. *, $P < 0.1$; **, $P < 0.01$; ***, $P < 0.001$. Error bars are standard deviations. Scale bars, 5µm.

Figure 4. Dynamics of polar landmarks and their relation to tip growth (A) Schematic representation of microtubule-dependent polarization. Tea1 is deposited at the cell surface by microtubules + end and recruits Tea4 that recruits the DYRK-family kinase Pom1. These landmarks act as key regulators of polarity in part by recruiting and activating downstream elements of actin-based polarity and trafficking. **(B)** Time-lapse of a WT cell expressing Tea1-3GFP and stained with fluorescent lectins growing over the cell cycle. The lectin signal is represented by dotted lines to facilitate the visualization of Tea1-3GFP **(C-E)** Evolution of the concentration of Tea1-3GFP (n=28 cells), Tea4-GFP (n= 42 cells) and Pom1-GFP (n= 38 cells) at the OE and the NE over the cell cycle. Bold lines represent the average and shades the standard deviations, from at least 2 independent experiments). **(F-H)** Tip growth speeds as a function of concentrations at cell poles for Tea1-3GFP, Tea4-GFP and Pom1-GFP for the OE and NE. Small dots in the background are single time-points from individual time-lapses. Large dots are binned

averages and error bars are standard deviations (see Material and methods for details on binning). Scale bars, 5μm.

Figure 5. Dynamics of polar F-actin and F-actin regulators and their relation to tip growth **(A)** Schematic representation of polar actin assembly. F-actin is present in both endocytic actin patches and cables. For actin assembly, active GTP-Cdc42 may recruit and activate multiple F-actin effectors, including the formin For3, which binds the actin-binding protein Bud6, and nucleates actin cables. **(B-E)** Evolution of the concentration of active-Cdc42 visualized by CRIB-GFP (n= 26 cells), For3-3GFP (n=32), Bud6-3GFP (n=44) and F-actin visualized with LifeAct-GFP (n= 44) at the OE and the NE over the cell cycle, and tip growth speeds plotted as a function of concentrations at cell poles for the same markers. Small dots in the background are single time-points from individual time-lapses. Large dots are binned averages and error bars are standard deviations (see Material and methods for details on binning).

Figure 6. Dynamics of upstream polar membrane and cell wall remodelers and their relation to tip growth (A) Schematic representation of secretory vesicle trafficking driven by Myosin Type V to the cell tips along actin cables. Vesicles fusion with the membrane is catalyzed by components of the exocyst, such as Sec8. Secretory vesicles carry enzymes for cell wall assembly, such as the β-glucan synthases, Bgs1 and Bgs4, which are regulated by the small GTPase Rho1, activated by the GEF Rgf1. **(B-G)** Evolution of the concentration of Myo52-3GFP (n= 38 cells), Sec8-GFP (n= 40), Active-Rho1 marked with ActRho1-Citrine (n= 34), GFP-Bgs1 (n=31), GFP-bgs4 (n=36) and Rgf1-GFP (n= 40) at the OE and the NE over the cell cycle, and tip growth speeds plotted as a function of concentration at cell poles for the same markers. Small dots in the background are single time-points from individual time-lapses. Large dots are binned averages and error bars are standard deviations (see Material and methods for details on binning).

Figure 7. Dependence of single tip growth speed on canonical surface remodelers in bipolar and monopolar cells. (A) Localization of indicated polar factors in WT vs *tea1Δ* monopolar cells growing from the OE or the NE. These cells were labeled with a fluorescent lectin, which is traced with dotted lines to facilitate the visualization of polar factors at cell tips. The fluorescence signal was contrasted and a noise filter was applied to all these images in the same manner, for better visualization. **(B-F)** Single tip growth speeds plotted as a function of concentration at cell

poles in WT vs *tea1Δ* monopolar cells at the OE and the NE, for GFP-bgs4 (WT, n=36 cells; *tea1Δ* OE, n=24*; tea1Δ*; NE, n=12), active GTP-Cdc42 marked with CRIB-GFP (WT, n=26; *tea1Δ* OE, n=25*; tea1Δ* NE, n=21), F-actin marked with LifeAct-GFP (WT, n=44; *tea1Δ* OE, n=30*; tea1Δ* NE, n=25), Myo52-3GFP (WT, n=38; *tea1Δ* OE, n=14*; tea1Δ* NE, n=16). The full and dotted lines represent the mean of binned data. Scale bars, 5 μm.

Figure 8. Dependence of single tip growth speed on Stipzenkörper concentration in fast growing *Aspergillus nidulans* hyphae. (A) Images of germlings and mature hyphae and the Spitzenkörper visualized with the post-golgi marker GFP-RabE^{Rab11}. **(B)** Segmentation of hyphal shapes and detection of growing poles with our image analysis platform. **(C)** Mean growth speed of germlings (n=15 cells) and mature hyphae (n=18). **(D)** Tip growth speeds plotted as a function of GFP-RabE^{Rab11} concentrations at cell pole for both germlings and mature hyphae. Small dots in the background are single time-points from individual time-lapses. Large dots are binned averages and error bars are standard deviations (see Material and methods for details on binning). Scale bars, 5 μm.

REFERENCES

Abenza, J. F., Couturier, E., Dodgson, J., Dickmann, J., Chessel, A., Dumais, J. and Carazo Salas, R. E. (2015). Wall mechanics and exocytosis define the shape of growth domains in fission yeast. *Nat Commun* **6**, 8400.

Atilgan, E., Magidson, V., Khodjakov, A. and Chang, F. (2015). Morphogenesis of the Fission Yeast Cell through Cell Wall Expansion. *Curr Biol* **25**, 2150-7.

Ayscough, K. R., Stryker, J., Pokala, N., Sanders, M., Crews, P. and Drubin, D. G. (1997). High rates of actin filament turnover in budding yeast and roles for actin in establishment and maintenance of cell polarity revealed using the actin inhibitor latrunculin-A. *The Journal of cell biology* **137**, 399-416.

Bastmeyer, M., Deising, H. B. and Bechinger, C. (2002). Force exertion in fungal infection. *Annu Rev Biophys Biomol Struct* **31**, 321-41.

Baumgartner, S. and Tolic-Norrelykke, I. M. (2009). Growth pattern of single fission yeast cells is bilinear and depends on temperature and DNA synthesis. *Biophys J* **96**, 4336-47.

Bendezu, F. O., Vincenzetti, V., Vavylonis, D., Wyss, R., Vogel, H. and Martin, S. G. (2015). Spontaneous Cdc42 polarization independent of GDI-mediated extraction and actin-based trafficking. *PLoS Biol* **13**, e1002097.

Bonazzi, D., Haupt, A., Tanimoto, H., Delacour, D., Salort, D. and Minc, N. (2015). Actin-Based Transport Adapts Polarity Domain Size to Local Cellular Curvature. *Curr Biol* **25**, 2677-83.

Bonazzi, D., Julien, J. D., Romao, M., Seddiki, R., Piel, M., Boudaoud, A. and Minc, N. (2014). Symmetry Breaking in Spore Germination Relies on an Interplay between Polar Cap Stability and Spore Wall Mechanics. *Dev Cell* **28**, 534-46.

Cadart, C., Monnier, S., Grilli, J., Saez, P. J., Srivastava, N., Attia, R., Terriac, E., Baum, B., Cosentino-Lagomarsino, M. and Piel, M. (2018). Size control in mammalian cells involves modulation of both growth rate and cell cycle duration. *Nat Commun* **9**, 3275.

Chang, F. and Martin, S. G. (2009). Shaping fission yeast with microtubules. *Cold Spring Harb Perspect Biol* **1**, a001347.

Das, M., Drake, T., Wiley, D. J., Buchwald, P., Vavylonis, D. and Verde, F. (2012). Oscillatory dynamics of Cdc42 GTPase in the control of polarized growth. *Science* **337**, 239-43.

Davi, V., Chevalier, L., Guo, H., Tanimoto, H., Barrett, K., Couturier, E., Boudaoud, A. and Minc, N. (2019). Systematic mapping of cell wall mechanics in the regulation of cell morphogenesis. *Proc Natl Acad Sci U S A* **116**, 13833-13838.

Davi, V. and Minc, N. (2015). Mechanics and morphogenesis of fission yeast cells. *Curr Opin Microbiol* **28**, 36-45.

Davì, V., Tanimoto, H., Ershov, D., Haupt, A., De Belly, H., Le Borgne, R., Couturier, E., Boudaoud, A. and Minc, N. (2018). Mechanosensation Dynamically Coordinates Polar Growth and Cell Wall Assembly to Promote Cell Survival. *Developmental Cell* **45**, 170-182.e7.

Di Gregorio, A., Bowling, S. and Rodriguez, Tristan A. (2016). Cell Competition and Its Role in the Regulation of Cell Fitness from Development to Cancer. *Developmental Cell* **38**, 621-634.

Haupt, A., Ershov, D. and Minc, N. (2018). A Positive Feedback between Growth and Polarity Provides Directional Persistency and Flexibility to the Process of Tip Growth. *Curr Biol* **28**, 3342-3351 e3.

Horio, T. and Oakley, B. R. (2005). The Role of Microtubules in Rapid Hyphal Tip Growth of Aspergillus nidulans. *Molecular Biology of the Cell* **16**, 918-926.

Horiseberger, M. and Rosset, J. (1977). Localization of alpha-Galactomannan on the surface of Schizosaccharomyces pombe cells by scanning electron microscopy. *Arch Microbiol* **112**, 123-6.

Horváth, A., Rácz-Mónus, A., Buchwald, P. and Sveiczer, Á. (2013). Cell length growth in fission yeast: an analysis of its bilinear character and the nature of its rate change transition. *FEMS Yeast Research* **13**, 635-649.

Howell, A. S., Savage, N. S., Johnson, S. A., Bose, I., Wagner, A. W., Zyla, T. R., Nijhout, H. F., Reed, M. C., Goryachev, A. B. and Lew, D. J. (2009). Singularity in polarization: rewiring yeast cells to make two buds. *Cell* **139**, 731-43.

Kelkar, M. and Martin, S. G. (2015). PKA antagonizes CLASP-dependent microtubule stabilization to re-localize Pom1 and buffer cell size upon glucose limitation. *Nat Commun* **6**, 8445.

Kinnaer, C., Dudin, O. and Martin, S. G. (2019). Yeast-to-hypha transition of Schizosaccharomyces japonicus in response to environmental stimuli. *Mol Biol Cell* **30**, 975-991.

Klumpp, S., Scott, M., Pedersen, S. and Hwa, T. (2013). Molecular crowding limits translation and cell growth. *Proceedings of the National Academy of Sciences* **110**, 16754-16759.

Knapp, B. D., Odermatt, P., Rojas, E. R., Cheng, W., He, X., Huang, K. C. and Chang, F. (2019). Decoupling of Rates of Protein Synthesis from Cell Expansion Leads to Supergrowth. *Cell Syst* **9**, 434-445 e6.

Köhli, M., Galati, V., Boudier, K., Roberson, R. W. and Philippsen, P. (2008). Growth-speed-correlated localization of exocyst and polarisome components in growth zones of Ashbya gossypii hyphal tips. *Journal of Cell Science* **121**, 3878-3889.

Lew, R. R. (2011). How does a hypha grow? The biophysics of pressurized growth in fungi. *Nat Rev Microbiol* **9**, 509-18.

Loewith, R. and Hall, M. N. (2011). Target of rapamycin (TOR) in nutrient signaling and growth control. *Genetics* **189**, 1177-1201.

López-Franco, R., Bartnicki-Garcia, S. and Bracker, C. E. (1994). Pulsed growth of fungal hyphal tips. *Proceedings of the National Academy of Sciences* **91**, 12228-12232.

Martin, S. G. (2015). Spontaneous cell polarization: Feedback control of Cdc42 GTPase breaks cellular symmetry. *Bioessays* **37**, 1193-201.

Martin, S. G. and Arkowitz, R. A. (2014). Cell polarization in budding and fission yeasts. *FEMS Microbiol Rev* **38**, 228-53.

Minc, N., Boudaoud, A. and Chang, F. (2009). Mechanical forces of fission yeast growth. *Curr Biol* **19**, 1096-101.

Mitchison, J. M. and Nurse, P. (1985). Growth in cell length in the fission yeast Schizosaccharomyces pombe. *J Cell Sci* **75**, 357-76.

Neurohr, G. E., Terry, R. L., Lengefeld, J., Bonney, M., Brittingham, G. P., Moretto, F., Miettinen, T. P., Vaites, L. P., Soares, L. M., Paulo, J. A. et al. (2019). Excessive Cell Growth Causes Cytoplasm Dilution And Contributes to Senescence. *Cell* **176**, 1083-1097.e18.

Nobs, J. B. and Maerkl, S. J. (2014). Long-term single cell analysis of S. pombe on a microfluidic microchemostat array. *PLoS One* **9**, e93466.

Pantazopoulou, A., Pinar, M., Xiang, X. and Peñalva, M. A. (2014). Maturation of late Golgi cisternae into RabERAB11 exocytic post-Golgi carriers visualized in vivo. *Molecular Biology of the Cell* **25**, 2428-2443.

Peñalva, M. A., Zhang, J., Xiang, X. and Pantazopoulou, A. (2017). Transport of fungal RAB11 secretory vesicles involves myosin-5, dynein/dynactin/p25, and kinesin-1 and is independent of kinesin-3. *Molecular Biology of the Cell* **28**, 947-961.

Perez-Gonzalez, N. A., Rochman, N. D., Yao, K., Tao, J., Le, M. T., Flanary, S., Sablich, L., Toler, B., Crentsil, E., Takaesu, F. et al. (2019). YAP and TAZ regulate cell volume. *J Cell Biol* **218**, 3472-3488.

Perez, P. and Cansado, J. (2010). Cell integrity signaling and response to stress in fission yeast. *Curr Protein Pept Sci* **11**, 680-92.

Perez, P. and Ribas, J. C. (2004). Cell wall analysis. *Methods* **33**, 245-51.

Qin, Y. and Yang, Z. (2011). Rapid tip growth: insights from pollen tubes. *Seminars in cell & developmental biology* **22**, 816-824.

Riquelme, M., Aguirre, J., Bartnicki-García, S., Braus, G. H., Feldbrügge, M., Fleig, U., Hansberg, W., Herrera-Estrella, A., Kämper, J., Kück, U. et al. (2018). Fungal Morphogenesis, from the Polarized Growth of Hyphae to Complex Reproduction and Infection Structures. *Microbiology and Molecular Biology Reviews* **82**, e00068-17.

Riquelme, M. and Bartnicki-Garcia, S. (2004). Key differences between lateral and apical branching in hyphae of Neurospora crassa. *Fungal Genetics and Biology* **41**, 842-851.

Russell, P. and Nurse, P. (1986). cdc25+ functions as an inducer in the mitotic control of fission yeast. *Cell* **45**, 145-53.

Soifer, I., Robert, L. and Amir, A. (2016). Single-Cell Analysis of Growth in Budding Yeast and Bacteria Reveals a Common Size Regulation Strategy. *Current Biology* **26**, 356-361.

Son, S., Tzur, A., Weng, Y., Jorgensen, P., Kim, J., Kirschner, M. W. and Manalis, S. R. (2012). Direct observation of mammalian cell growth and size regulation. *Nature Methods* **9**, 910-912.

Steinberg, G., Penalva, M. A., Riquelme, M., Wosten, H. A. and Harris, S. D. (2017). Cell Biology of Hyphal Growth. *Microbiol Spectr* **5**.

Tatebe, H., Nakano, K., Maximo, R. and Shiozaki, K. (2008). Pom1 DYRK regulates localization of the Rga4 GAP to ensure bipolar activation of Cdc42 in fission yeast. *Curr Biol* **18**, 322-30.

Uyttewaal, M., Burian, A., Alim, K., Landrein, B., Borowska-Wykręt, D., Dedieu, A., Peaucelle, A., Ludynia, M., Traas, J., Boudaoud, A. et al. (2012). Mechanical Stress Acts via Katanin to Amplify Differences in Growth Rate between Adjacent Cells in Arabidopsis. *Cell* **149**, 439-451.

Weiss, R. L., Kukora, J. R. and Adams, J. (1975). The relationship between enzyme activity, cell geometry, and fitness in Saccharomyces cerevisiae. *Proceedings of the National Academy of Sciences* **72**, 794-798.

Wu, C. F. and Lew, D. J. (2013). Beyond symmetry-breaking: competition and negative feedback in GTPase regulation. *Trends Cell Biol* **23**, 476-83.

Yuan, H.-X., Xiong, Y. and Guan, K.-L. (2013). Nutrient sensing, metabolism, and cell growth control. *Molecular cell* **49**, 379-387.

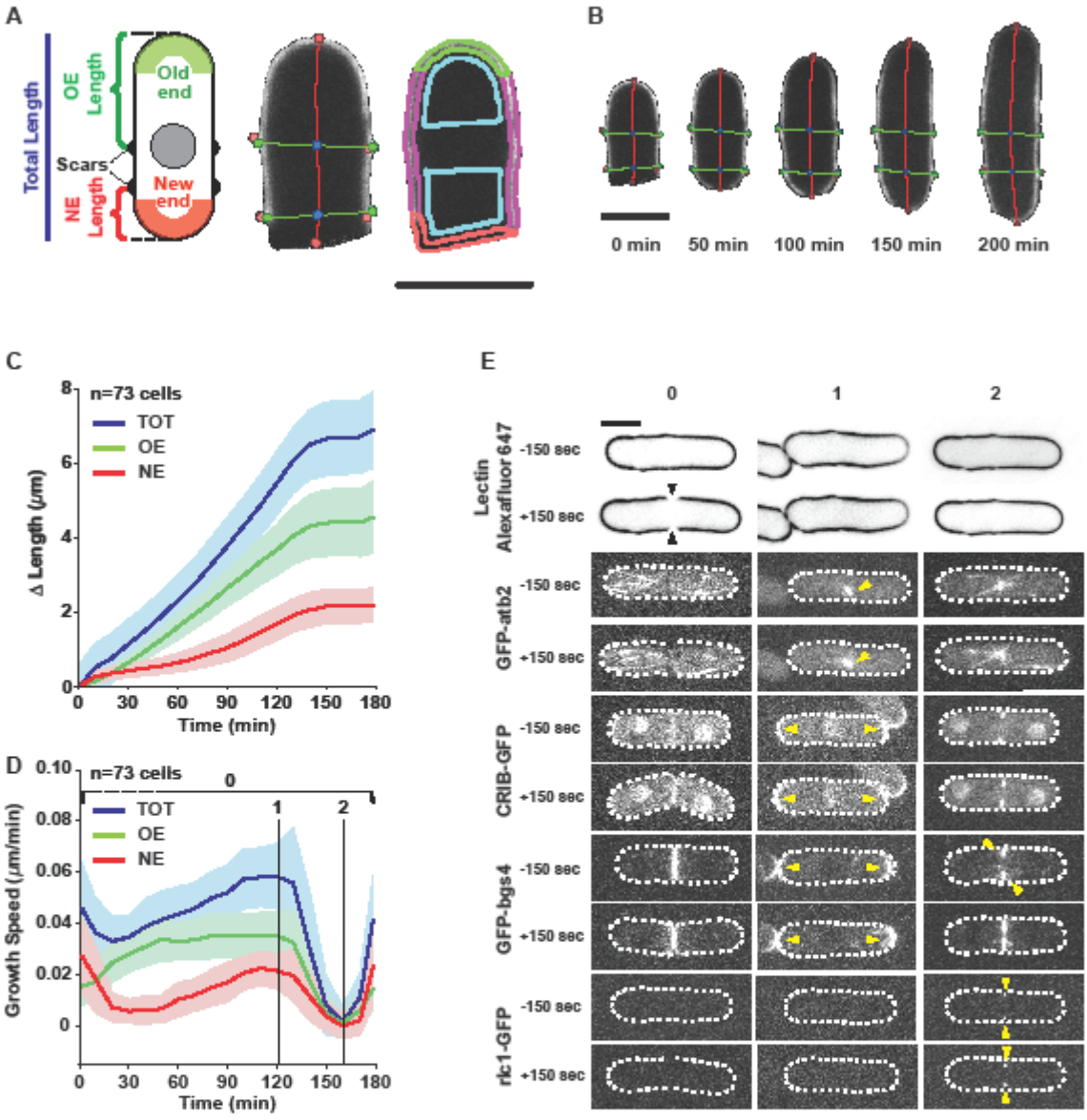
A
Total Length
OE Length
Old end
Scars
NE Length
New end
B
0 min
50 min
100 min
150 min
200 min
C
n=73 cells
TOT
OE
NE
Δ Length (μm)
Time (min)
D
n=73 cells
TOT
OE
NE
Growth Speed (μm/min)
Time (min)
E
Lectin Alexafluor 647
GFP-atb2
CRIB-GFP
GFP-bgs4
rlc1-GFP
-150 sec
+150 sec

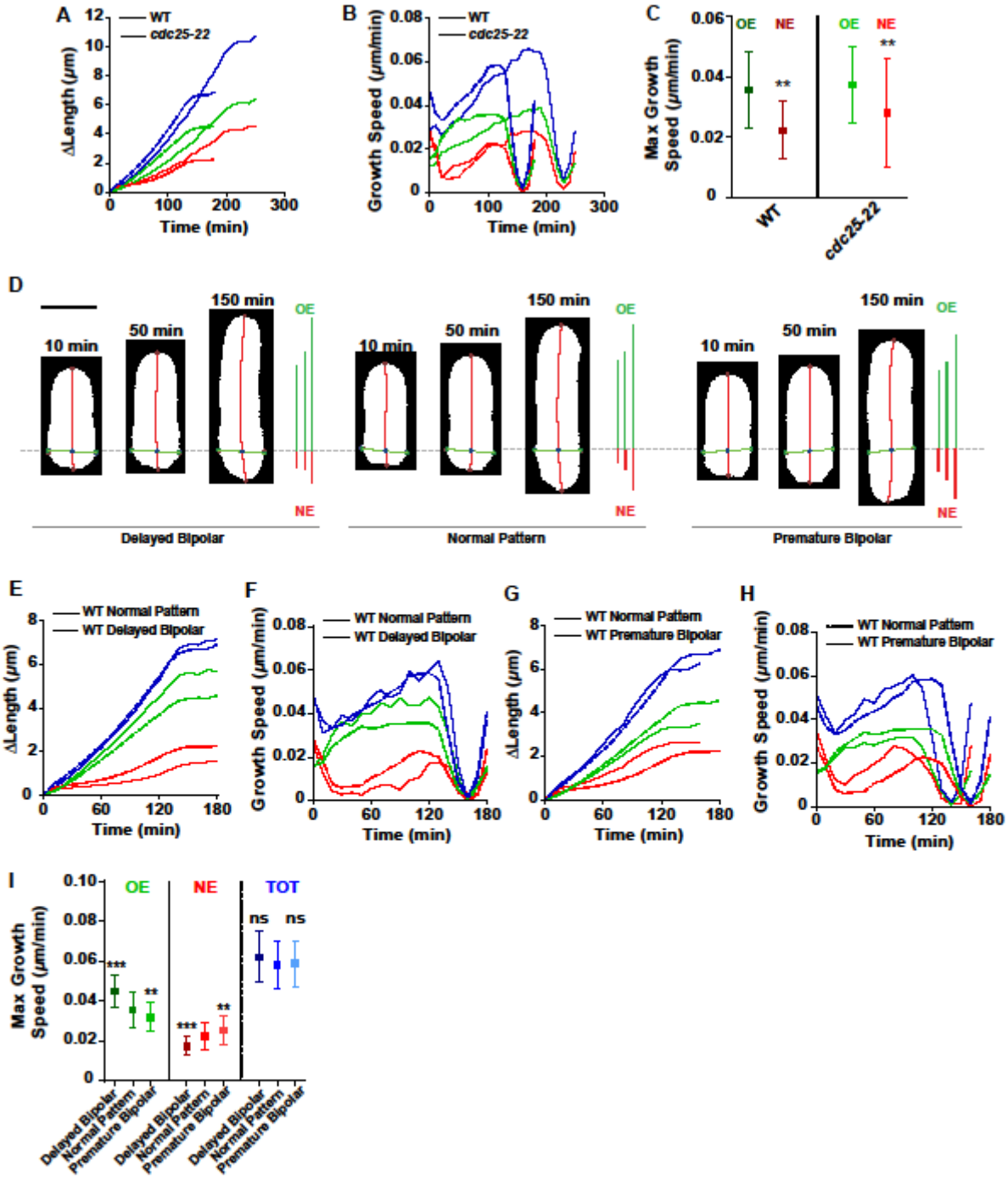
A
WT
cdc25-22
ΔLength (μm)
Time (min)
B
Growth Speed (μm/min)
C
Max Growth Speed (μm/min)
OE
NE
WT
cdc25-22
D
10 min
50 min
150 min
Delayed Bipolar
Normal Pattern
Premature Bipolar
E
WT Normal Pattern
WT Delayed Bipolar
F
G
WT Premature Bipolar
H
I
TOT
ns
Delayed Bipolar
Normal Pattern
Premature Bipolar

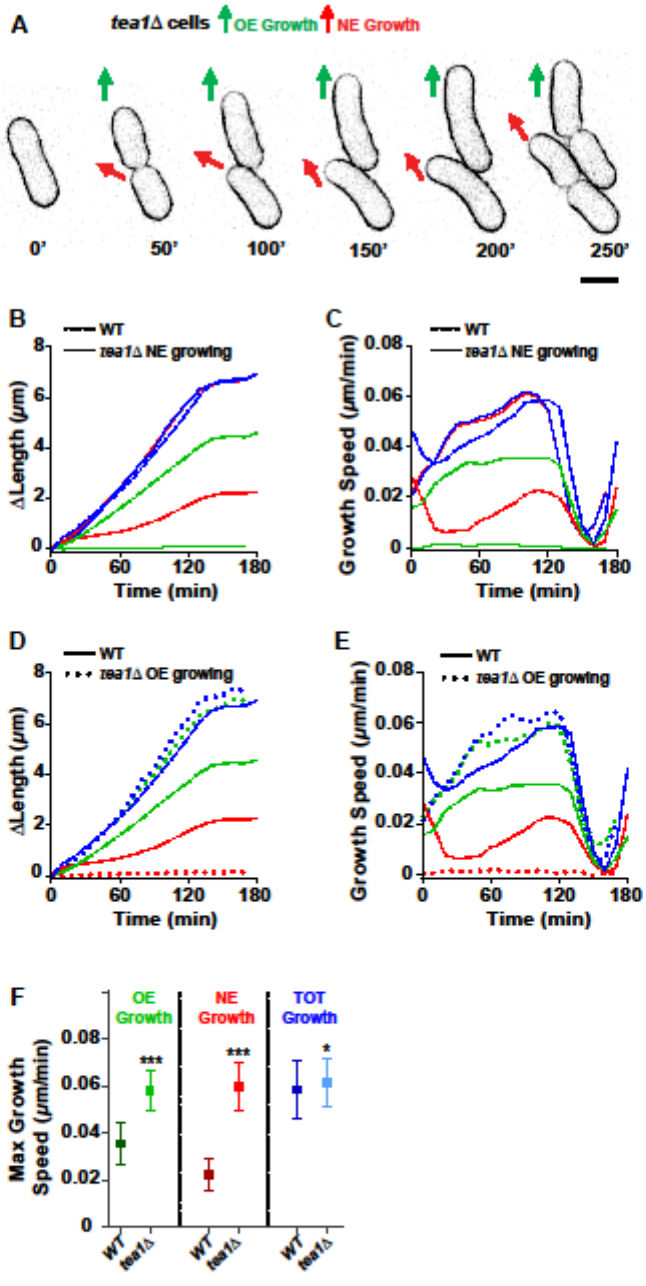
A
tea1Δ cells
OE Growth
NE Growth
0'
50'
100'
150'
200'
250'
B
WT
tea1Δ NE growing
ΔLength (μm)
Time (min)
C
WT
tea1Δ NE growing
Growth Speed (μm/min)
Time (min)
D
WT
tea1Δ OE growing
ΔLength (μm)
Time (min)
E
WT
tea1Δ OE growing
Growth Speed (μm/min)
Time (min)
F
OE Growth
NE Growth
TOT Growth
Max Growth Speed (μm/min)
WT
tea1Δ

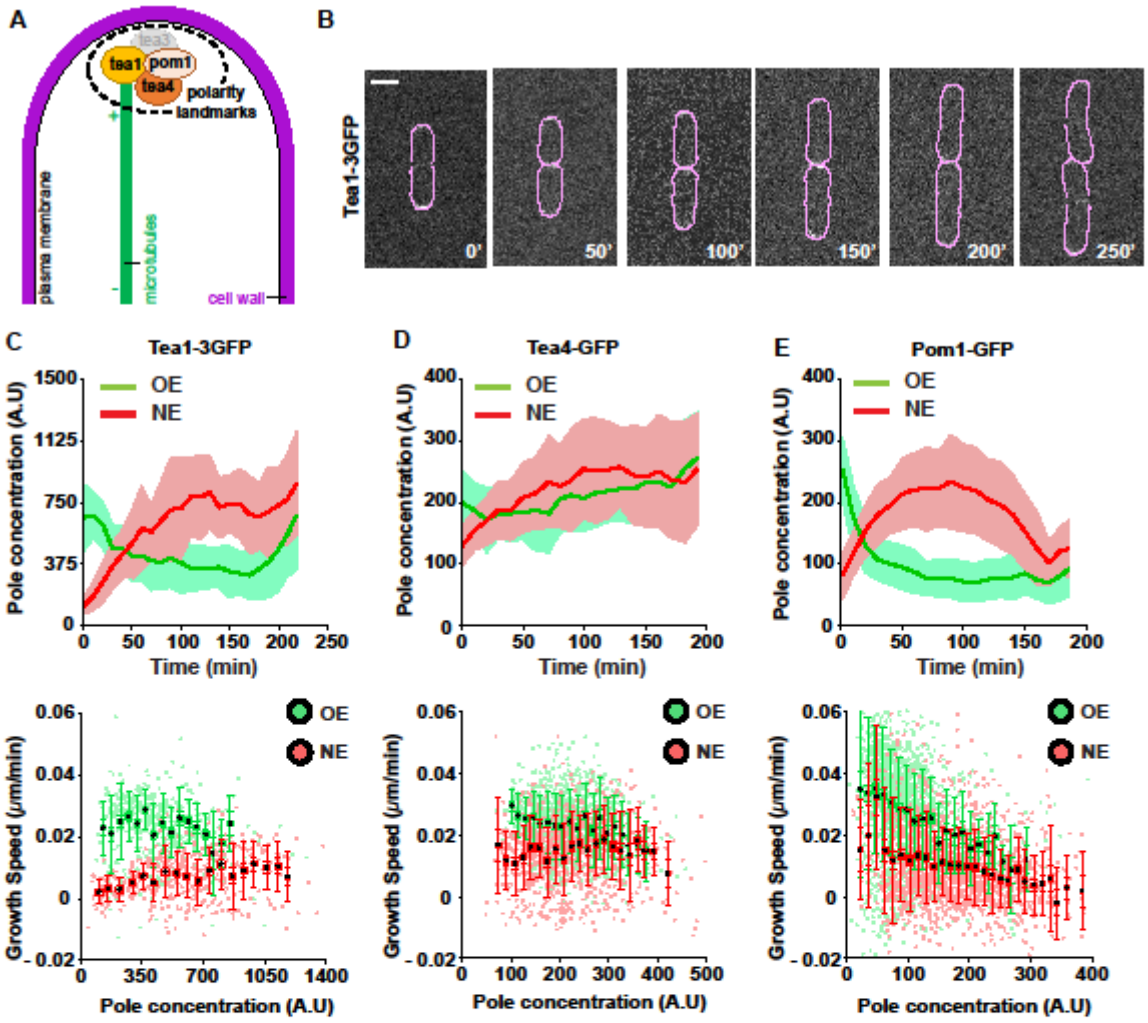
A
tea3
tea1
pom1
tea4
polarity
landmarks
plasma membrane
microtubules
cell wall
B
Tea1-3GFP
0'
50'
100'
150'
200'
250'
C
Tea1-3GFP
OE
NE
Pole concentration (A.U)
Time (min)
Growth Speed (μm/min)
Pole concentration (A.U)
D
Tea4-GFP
E
Pom1-GFP

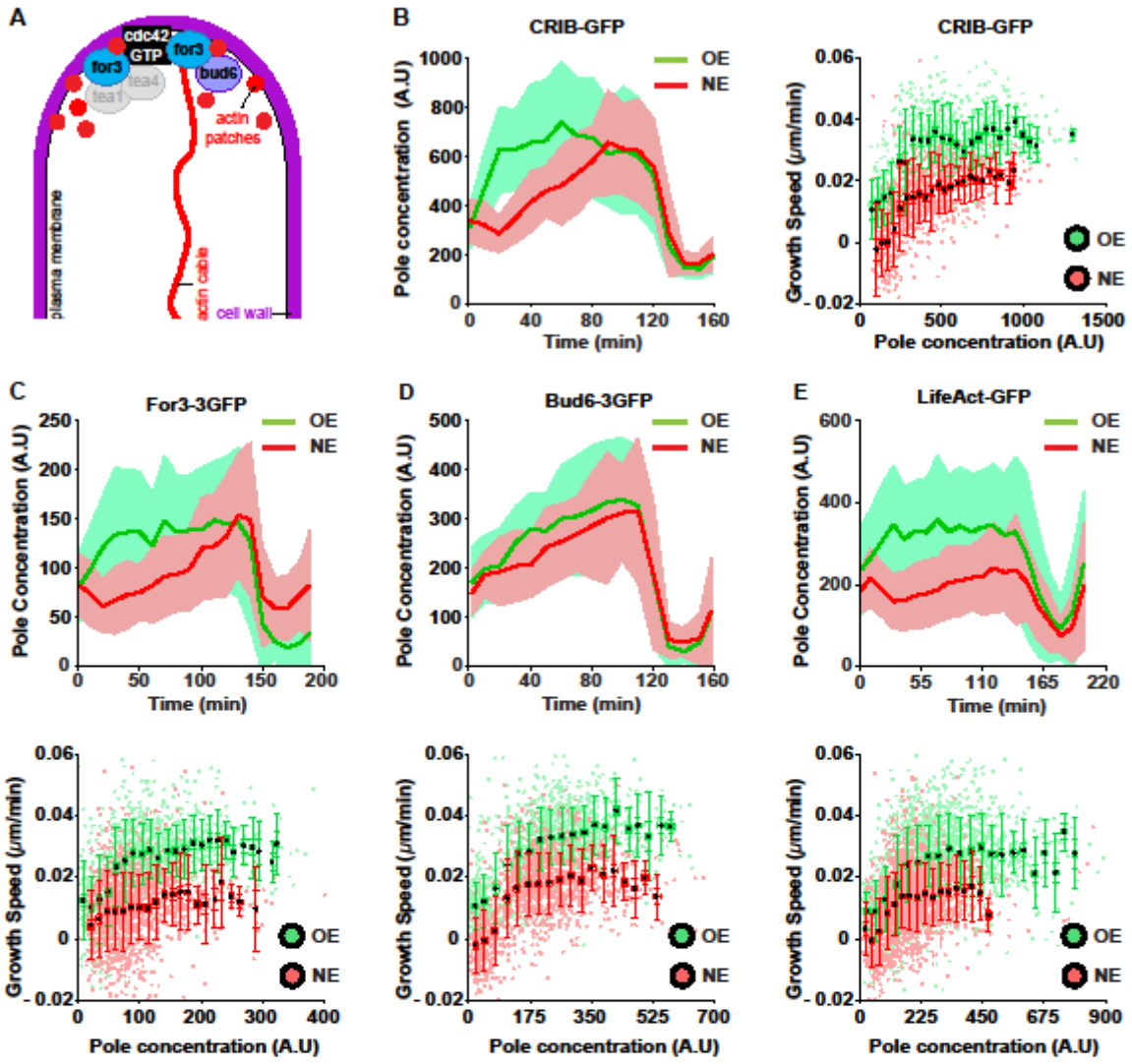
A
cdc42
GTP
for3
for3
bud6
tea1
tea4
actin patches
plasma membrane
actin cable
cell wall
B
CRIB-GFP
OE
NE
Pole concentration (A.U)
Time (min)
CRIB-GFP
Growth Speed (μm/min)
Pole concentration (A.U)
C
For3-3GFP
D
Bud6-3GFP
E
LifeAct-GFP

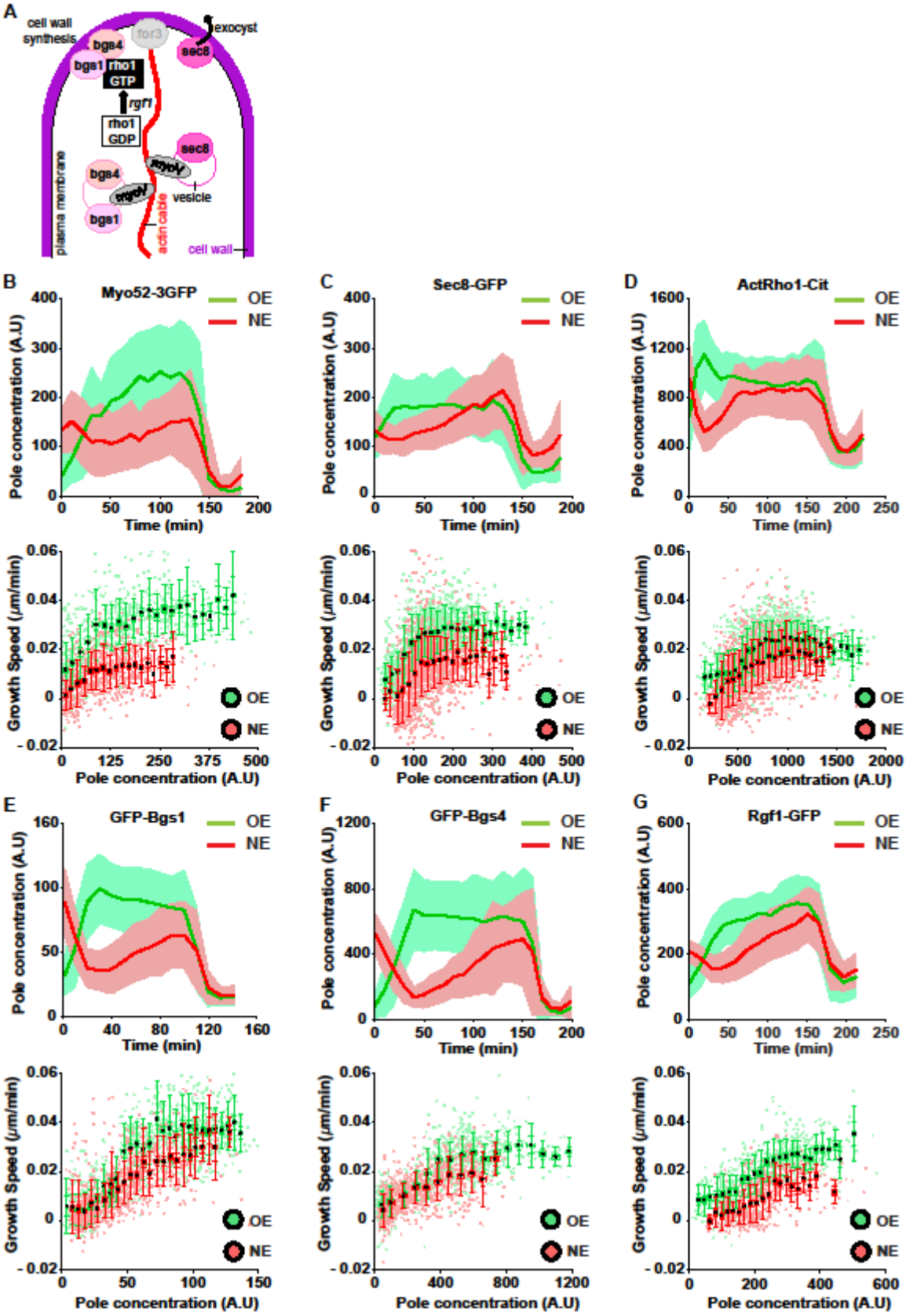
A
cell wall synthesis
bgs4
for3
exocyst
sec8
bgs1
rho1 GTP
rgf1
rho1 GDP
sec8
myo2
bgs4
myo1
vesicle
bgs1
actin cable
plasma membrane
cell wall
B
Myo52-3GFP
OE
NE
Pole concentration (A.U)
Time (min)
Growth Speed (μm/min)
Pole concentration (A.U)
C
Sec8-GFP
D
ActRho1-Cit
E
GFP-Bgs1
F
GFP-Bgs4
G
Rgf1-GFP

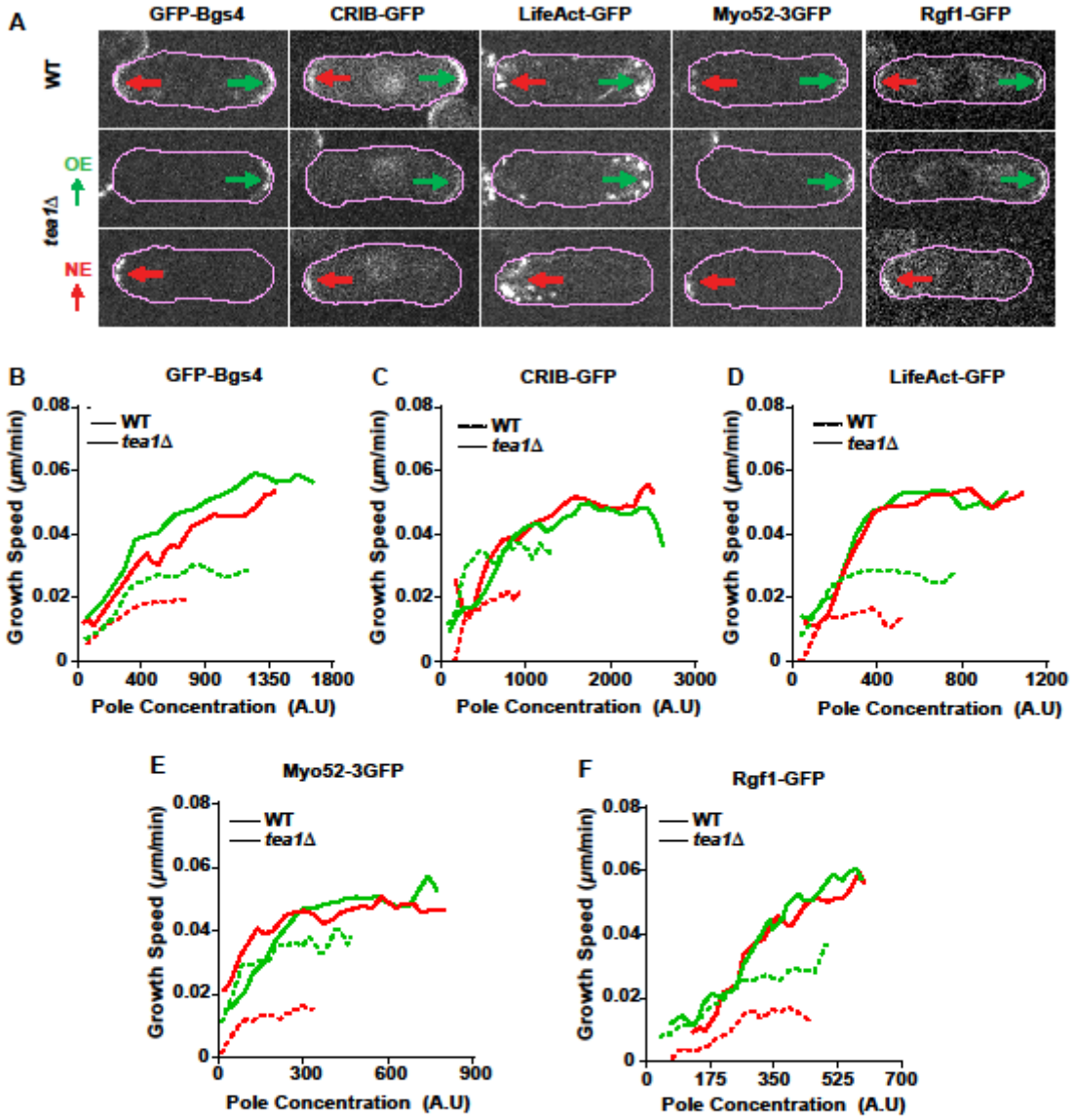
A
GFP-Bgs4
CRIB-GFP
LifeAct-GFP
Myo52-3GFP
Rgf1-GFP
WT
OE
tea1Δ
NE
B
GFP-Bgs4
C
CRIB-GFP
D
LifeAct-GFP
WT
tea1Δ
Growth Speed (μm/min)
Pole Concentration (A.U)
E
Myo52-3GFP
F
Rgf1-GFP

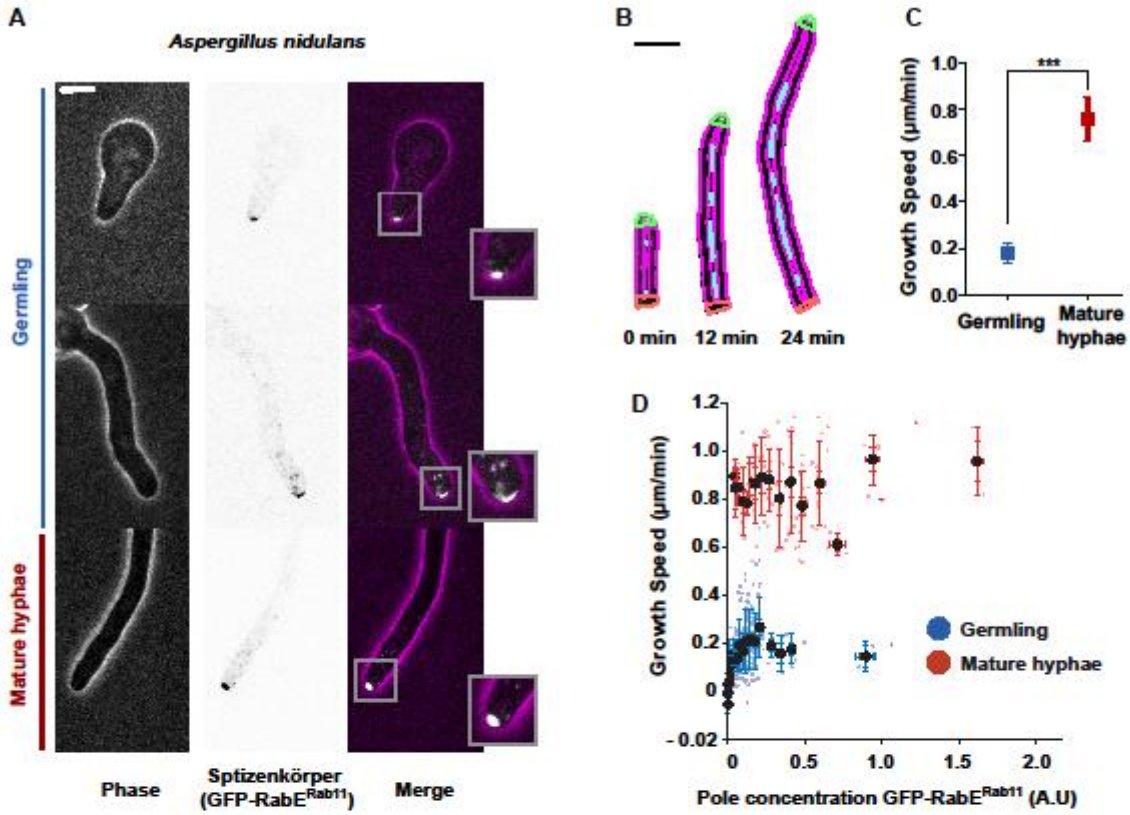
A
Aspergillus nidulans
Germling
Mature hyphae
Phase
Sptizenkörper
(GFP-RabE^Rab11)
Merge
B
0 min
12 min
24 min
C
Growth Speed (µm/min)
1.0
0.8
0.6
0.4
0.2
0.0
***
Germling
Mature hyphae
D
Growth Speed (µm/min)
1.2
1.0
0.8
0.6
0.4
0.2
0
- 0.02
0
0.5
1.0
1.5
2.0
Germling
Mature hyphae
Pole concentration GFP-RabE^Rab11 (A.U)